Measurement Science and Technology

Inverse solutions for electrical impedance tomography based on conjugate gradients methods

To cite this article: M Wang 2002 *Meas. Sci. Technol.* **13** 101

Meas. Sci. Technol. **13** (2002) 101–117 PII: S0957-0233(02)26552-2

Inverse solutions for electrical impedance tomography based on conjugate gradients methods

M Wang

School of Process, Environmental and Materials Engineering, University of Leeds, Leeds LS2 9JT, UK

E-mail: minmw@leeds.ac.uk

Received 5 July 2001, in final form 9 October 2001, accepted for publication 24 October 2001
Published 12 December 2001
Online at stacks.iop.org/MST/13/101

Abstract
A multistep inverse solution for two-dimensional electric field distribution is developed to deal with the nonlinear inverse problem of electric field distribution in relation to its boundary condition and the problem of divergence due to errors introduced by the ill-conditioned sensitivity matrix and the noise produced by electrode modelling and instruments. This solution is based on a normalized linear approximation method where the change in mutual impedance is derived from the sensitivity theorem and a method of error vector decomposition. This paper presents an algebraic solution of the linear equations at each inverse step, using a generalized conjugate gradients method. Limiting the number of iterations in the generalized conjugate gradients method controls the artificial errors introduced by the assumption of linearity and the ill-conditioned sensitivity matrix. The solution of the nonlinear problem is approached using a multistep inversion. This paper also reviews the mathematical and physical definitions of the sensitivity back-projection algorithm based on the sensitivity theorem. Simulations and discussion based on the multistep algorithm, the sensitivity coefficient back-projection method and the Newton–Raphson method are given. Examples of imaging gas–liquid mixing and a human hand in brine are presented.

Keywords: electrical impedance tomography, sensitivity theorem, inverse solution, conjugate gradients method

(Some figures in this article are in colour only in the electronic version)

1. Introduction

Geselowitz (1971) and Lehr (1972) derived the change of mutual impedance in relation to a change of conductivity in a four-terminal system used for impedance plethysmography; this is referred to as the lead theorem or the sensitivity theorem (Murai and Kagawa 1985, Yorkey *et al* 1987). Murai and Kagawa suggested a linear approximation, based on ignoring the high-order terms with respect to $\Delta\sigma$ (see appendix A.1). This linear approximation enables the use of iterative techniques to solve the nonlinear problem in electrical impedance computed tomography. Murai and Kagawa also reported an iterative method designed to solve the nonlinear inverse problem. The sensitivity theorem has been widely used for image reconstruction in electrical impedance tomography (EIT) (Williams and Beck 1995), particularly the single-step method based on the sensitivity coefficient back-projection (SBP) method (Kotre 1994) and the Newton one-step reconstruction (NOSER) method (Cheney *et al* 1990). In industrial applications of EIT, reconstructed images are affected by errors in electrode modelling and by measurement noise. In practice, it is difficult to make the electrode system fully consistent (variations in geometry, electrode–electrolyte interface, installation environment, etc). The quality of data acquired in industrial environments often deteriorates because of industrial and instrument noise. Normalization or regularization procedures are therefore employed in almost all back-projection algorithms. Based on the expressions for mutual impedance and the change in mutual impedance in the sensitivity theorem, a normalized expression, as given in equation (1) (Wang *et al* 1999), can be derived from dividing (A.5) by (A.6) (see appendix A.1). Equation (1) is used as a core equation for the following discussion

$$\frac{\Delta V_j}{V_j} \approx -\frac{\sum_{k=1}^{w} \Delta\sigma_k s_{j,k}(\sigma_k)}{\sum_{k=1}^{w} \sigma_k s_{j,k}(\sigma_k)} \quad (\Delta\sigma_k \ll \sigma_k,\ j = 1, 2, \ldots, P) \tag{1}$$

where j is the location of the measurement-projection, k is the pixel number, $s_{j,k}$ denotes the sensitivity coefficient at pixel k under the measurement-projection j, P denotes the maximum number of measurements, w denotes the maximum number of pixels, σ_k and $\Delta\sigma_k$ are the conductivity and conductivity change respectively at pixel k, and V_j and ΔV_j refer to the reference voltage and the voltage change at measurement-projection j.

A number of multistep iterative methods for solving the inverse problem of a nonlinear electric field using the solution of a linear approximation at each step have been reported (Boone *et al* 1997), in particular the compensation methods based on the sensitivity theorem (Murai and Kagawa 1985) and the Newton–Raphson (NR) method (Yorkey *et al* 1987). The artificial errors or imaging divergence introduced into the reconstructed conductivity distribution are noted as the product of the ill-conditioned matrix in the inverse problem. The artificial errors may be minimized by applying some regularization techniques to the solution procedure, such as the singular value decomposition (SVD) method and Akaike's information criterion (Akaike 1974), the Marquardt method (Marquardt 1963) and the Tikhonov regularization method (Vauhkonen *et al* 1998, Lionheart 2001).

The conjugate gradients (CG) method, based on its convergence characteristics, is one of the best known iterative methods (Reid 1971) for solving a large system of linear equations with an $N \times N$ symmetrical and positively defined sparse coefficient matrix. Application of CG methods in tomography techniques have been reported but these applications were purely for solving linear equations (Woo *et al* 1993, Arridge and Schweiger 1998, Player *et al* 1999). However, in EIT, not only an ill-conditioned matrix but also the linear assumption can result in the problem of divergence, since the linear approximation is only valid for a small conductivity change. Instead of looking for a precise solution in the use of direct methods, such as the Cholesky decomposition method, the CG method searches for a minimized residual by applying a number of iterations. The use of CG with controlled iterations in each linear inverse step, as reported in this paper, can produce an optimized approximation for solving the nonlinear problem with multisteps. The solution procedure in CG, based on vector operation and updating, may also provide an attractive opportunity for the use of parallel and vector computing (Carey 1989) for three-dimensional (3D) EIT imaging.

This paper presents a multistep inverse solution based on an approximate solution of the linear equation (1) using a generalized conjugate gradients (GCG) method and a method of error vector decomposition. The mathematical and physical definitions of the sensitivity back-projection (SBP) algorithm are also reviewed in order to understand the advantages, suitability and impacts of applying the SBP further.

2. Inverse solutions

2.1. Sensitivity theorem-based inverse solution using conjugate gradients methods

The 'absolute value' reconstruction algorithms, such as the NR method and the compensation method, work very well with contamination-free data. However, their reconstruction convergence can often not be achieved if the data come with a certain level of electrode error and instrument noise. To deal with noisy data in industrial applications, the normalized expression of the sensitivity theorem, as set out in equation (1), is adopted for regularization of the sensitivity matrix and reduction of the electrode error in a multistep inverse solution. The problem of conductivity distribution is of a nonlinear type. As the sensitivity theorem is based on a linear approximation with the condition $\Delta\sigma \ll \sigma$, an iterative approach is therefore employed in many cases to approach the true value. The procedures for both the forward and inverse solution have to be employed in the multistep solution for updating the conductivity and sensitivity matrices and error estimation, resulting in a step solution.

Forward solution. The forward solution in the multistep inverse solution is employed for producing an error vector for the inverse solution in each step. It also updates the sensitivity matrix for the inverse solution in the next step. The sensitivity matrix can be derived from the nodal voltages obtained in the forward solution (Murai and Kagawa 1985, Yorkey *et al* 1987). The actual current value used in the solution is not significant, as long as the value does not vary throughout the whole process, since only relative changes in the boundary voltage measurements are employed.

A finite element method (FEM) model presenting a two-dimensional (2D) cross-section of a process vessel with Neumann boundary conditions in addition to a single Dirichlet condition to avoid singularity can be solved by equation (2) (Murai and Kagawa 1985, Yorkey *et al* 1987)

$$\boldsymbol{Y}\boldsymbol{v} = \boldsymbol{c} \tag{2}$$

where $\boldsymbol{Y}$, $\boldsymbol{v}$, $\boldsymbol{c}$ denotes the global admittance matrix, the nodal voltage vector, and the nodal current vector respectively.

The ordinary CG method ((A.12) in appendix A.2) can be applied to solve the linear equations in the forward problem efficiently, since the global admittance matrix is a symmetrical and positively defined sparse matrix (Abdullah 1993). The construction method of the global admittance matrix was detailed by Murai and Kagawa (1985).

Inverse solution. Based on the expression given by equation (1) and the assumption of a homogeneous conductivity distribution, σ_0, at the time of taking reference

V, the inverse solution in the multistep approach is given by equation (3) in the form of matrix notation

$$\gamma = -\bar{s}^{-1} \cdot e \tag{3}$$

where the elements of the normalized sensitivity matrix, $\bar{s}^{-1}$ at the iteration n, the vector of relative conductivity change, γ, at pixel k, and the vector of relative boundary change, e, at projection j are denoted as equations (4)–(6) respectively. The conductivity is updated by equation (7):

$$\bar{s}_{j,k}^{(n)} = \frac{s_{j,k}(\hat{\sigma}_k^{(n)})}{\sum_{k=1}^{w} s_{j,k}(\hat{\sigma}_k^{(0)})} \tag{4}$$

$$\gamma_k^{(n+1)} = \frac{\Delta\hat{\sigma}_k^{(n+1)}}{\hat{\sigma}_k^{(0)}} \tag{5}$$

$$e_j^{(n)} = \frac{\Delta V}{V} = \frac{V_j'(\sigma') - V_j(\sigma)}{V_j(\sigma)} = \frac{V_j'(\sigma')}{V_j(\sigma)} - \frac{V_j(\sigma)}{V_j(\sigma)} \tag{6}$$

$$\hat{\sigma}_k^{(n+1)} = \hat{\sigma}_k^{(n)}(1 + \gamma_k^{(n+1)}) \tag{7}$$

where σ and σ' are the actual conductivity distributions at the moment of acquiring the reference voltage V and measurement V'. $\hat{\sigma}_k^{(0)}$ and $\hat{\sigma}_k^{(n)}$ are the estimated conductivity values for simulating σ and σ'.

Since conductivity is inversely related to voltage, conductivity updating can also be based on an approximation of the inverse relation (equation (8) based on $1+x \approx 1/(1-x)$ at $x < 1$), which can improve the convergence speed for both positive and negative changes in conductivity

$$\hat{\sigma}_k^{(n+1)} \approx \frac{\hat{\sigma}_k^{(n)}}{1 - \gamma_k^{(n+1)}}. \tag{8}$$

Noting the validating condition $\Delta\sigma \ll \sigma$, the $s_{j,k}(\hat{\sigma}_k^{(0)})$ in response to $u_j(\hat{\sigma}_k^{(0)})$ as well as the regularization procedure in the linear approximation equations (1), (6) thus decomposes to

$$e_j^{(n)} = \frac{V_j'(\sigma')}{V_j(\sigma)} - \frac{u_j'(\hat{\sigma}_k^{(n)})}{u_j(\hat{\sigma}_k^{(0)})} \tag{9}$$

where $u_j(\hat{\sigma}_k^{(0)})$ and $u_j'(\hat{\sigma}_k^{(n)})$ are the computed reference voltage and measurement voltage with respect to the conductivity distribution $\hat{\sigma}_k^{(0)}$ and $\hat{\sigma}_k^{(n)}$. At the initial stage, the $u_j'(\hat{\sigma}_k^{(n)})$ is the same as the $u_j(\hat{\sigma}_k^{(0)})$, therefore equation (9) is equivalent to equation (6). After a number of steps of updating the conductivity distribution and the sensitivity matrix, the decomposed relative boundary change or error vector given by equation (9) will be minimized, which means that the computed relative change is close to the measured relative change. It is thought that the nonlinear inverse solution has been reached when the norm of the error vector is sufficiently small.

The error function decomposition method, which examines the differences between relative changes in the measured and simulated voltages, has the following benefits:

- It transforms the relative changes from a measurement domain to a simulation domain, so can greatly reduce the effect of electrode modelling errors (e.g. the errors due to the inconsistency of electrode size, geometry, position, etc (Wang *et al* 1999)).
- It may eliminate, or minimize, the effect of instrumentation/environmental errors (e.g. bias, gain error, etc).
- It can subtract the high contrast of the background (e.g. a metal impeller in mixing process) from the reconstructed image and therefore highlight the low-contrast change in the region interest.
- It can 'transform' 3D measurement patterns to 2D measurement patterns in order to adapt a 2D reconstruction algorithm (due to the use of relative changes).

As the sensitivity matrix is, in its general form, neither symmetrical nor square, the ordinary CG method and the GCG method (of biconjugate gradients or minimum residuals) could not be directly applied for the solution of equation (3). For an unsymmetric $M \times N$ sensitivity matrix, $\bar{s}(M \neq N)$, the minimization function shown as equation (11) below can be derived by minimizing equation (10):

$$f(\gamma) = \tfrac{1}{2}\|\bar{s} \cdot \gamma + e\|^2 \tag{10}$$

$$\nabla f = r_0 = \bar{s}^{\mathrm{T}} \cdot (\bar{s} \cdot \gamma + e). \tag{11}$$

The CG method may be applied to the transformed equation (11) without forming $\bar{s}^{\mathrm{T}}\bar{s}$ explicitly (Jennings and McKeown 1992) or using (A.12) (in appendix A.2) except where u_k is replaced by equation (12).

$$u_k = A^{\mathrm{T}}(Ap_k). \tag{12}$$

Although this transformation makes the GCG methods applicable for the solution of equation (3), it should be noted that $\bar{s}^{\mathrm{T}}\bar{s}$ is much more ill-conditioned than $\bar{s}$. A large condition number increases the number of iterations required in the use of the GCG, and limits the accuracy by which a solution can be obtained (Press *et al* 1992). Moreover, due to the linear assumption in equation (1), if the relative change in conductivity is large there could be significant artificial errors. The pixels/areas most likely to be affected are those with small eigenvalues or low sensitivity. In fact, the regularization factor used in direct solution methods, such as Cholesky decomposition, produces an approximate solution with less effect on these pixels at each inverse step, thus minimizing such artificial error. The regularization factor generally decreases when the solution is close to the true value or the linear approximation is more validated (Yorkey *et al* 1987). Unlike direct methods for a precise solution, the GCG method searches for the minimized residual by applying a number of iterations. An approximate solution for equation (1) can always be made at each step, if a certain residual is kept to within a limited number of iterations. The nonlinear solution can be reached by multistep inversion, with either a fixed iteration number or a generally increased number of iterations at each inverse step according the size of the errors. Correct selection of the number of iterations can speed up the rate of convergence and reduce the artificial noise caused by the linear assumption and the ill-conditioned sensitivity matrix; this will be further discussed in the next section. For convenience in this discussion, the acronym SCG (sensitivity theorem based inverse solution using CG methods) is employed.

The inverse solution is obtained following the procedure given below.

(1) Pre-compute the assumed boundary voltage vector and the sensitivity matrix

$$\boldsymbol{u}(\hat{\boldsymbol{\sigma}}^{(0)}) \qquad \boldsymbol{s}(\hat{\boldsymbol{\sigma}}^{(0)}).$$

(2) Measure the boundary voltage profiles and produce the relative change vector

$$\eta_j = \frac{V'_j(\sigma')}{V_j(\sigma)} \qquad (j = 1, 2, \ldots, P).$$

(3) Preset the iteration control factors for the minimum convergence error, ε_s, the maximum number of inverse steps, δ_s, and the maximum number of iterations, δ_c, for the GCG.

(4) Initiate the first estimations for the error function vector and the conductivity vector

$$\boldsymbol{e}^{(1)} = \left[e_1^{(1)}, \ldots, e_P^{(1)}\right]^{\mathrm{T}} \qquad e_j^{(1)} = \eta_j - \sum_{j=1}^{P} \eta_j / P$$

$$\hat{\sigma}^{(1)} = \left[\hat{\sigma}_1^{(1)}, \ldots, \hat{\sigma}_w^{(1)}\right]^{\mathrm{T}} \qquad \hat{\sigma}_k^{(1)} = \sigma_0 \Big/ \sum_{j=1}^{P} \eta_j / P.$$

(5) Normalize the sensitivity matrix (the iteration steps n go from 1 to δ_s)

$$\bar{s}_{j,k}^{(n)} = \frac{s_{j,k}(\hat{\sigma}_k^{(n)})}{\sum_{k=1}^{w} s_{j,k}(\hat{\sigma}_k^{(0)})}.$$

(6) Solve the inverse problem using the GCG method and then update the relative change in the conductivity vector (maximum iteration $= \delta_c$)

$$\gamma = -\bar{\boldsymbol{s}}^{-1} \cdot \boldsymbol{e}.$$

(7) Update the conductivity vector

$$\hat{\boldsymbol{\sigma}}^{(n+1)} = \hat{\boldsymbol{\sigma}}^{(n)} \cdot (1 + \gamma^{(n+1)}).$$

(8) Solve the forward problem using the ordinary CG method to update the boundary voltage vector and sensitivity matrix

$$\boldsymbol{u}(\hat{\boldsymbol{\sigma}}^{(n+1)}) \qquad \boldsymbol{s}(\hat{\boldsymbol{\sigma}}^{(n+1)}).$$

(9) Update the error vector

$$e_j^{(n+1)} = \eta_j - \frac{u'_j(\hat{\boldsymbol{\sigma}}_k^{(n+1)})}{u_j(\hat{\boldsymbol{\sigma}}_k^{(0)})}.$$

(10) Check whether one of the control factors has been reached

$$\|\bar{e}\| \leqslant \varepsilon_s \qquad \text{or} \qquad \text{Steps} \geqslant \delta_s?$$

(11) If convergence or the maximum number of iterations is not reached, the process jumps to step (5) until one of these conditions is reached.

2.2. *Definition of the sensitivity coefficient back-projection algorithm*

The sensitivity coefficient back-projection approximation method (SBP), using a normalized transpose matrix of the sensitivity matrix obtained from (A.7) (in appendix A.1) as a weighting matrix, was first defined by Breckon and Pidcock (1987) and refined for EIT by Kotre (1994). The approximation has been successfully applied to many industrial applications (Williams and Beck 1995), because of its simplicity, good antinoise capability and fast solution speed. Lionheart (2001) has explained how the mathematical approximation can be made by applying a value of zero as the initial estimate in the first iteration of Landweber's iterative method (Landweber 1951) and why the crude reconstruction algorithm (SBP) can be derived 'using the transpose as an approximate inverse'. To solve $\boldsymbol{A}\boldsymbol{x} = \boldsymbol{b}$, the nth Landweber iteration gives the next estimate as

$$\boldsymbol{x}_n = \boldsymbol{x}_{n-1} - \boldsymbol{\tau}\boldsymbol{A}^{\mathrm{T}}(\boldsymbol{A} \cdot \boldsymbol{x}_{n-1} - \boldsymbol{b}) \qquad (13)$$

where $\boldsymbol{\tau}$ is a diagonal relaxation matrix in which its diagonal parameter satisfies $0 < \tau_{jj} < 2/\lambda_j^2$ and λ is the eigenvector of $\boldsymbol{A}$. If $x_0 = 0$ is the initial estimate, then the first approximation to equation (13) is $\boldsymbol{\tau}\boldsymbol{A}^{\mathrm{T}}\boldsymbol{b}$. A version of Landweber's iterative method has been used for capacitance tomography (Yang *et al* 1999).

The transformed matrix, $\bar{\boldsymbol{s}}^{\mathrm{T}}\bar{\boldsymbol{s}}$, presents the pixels' correlation in EIT, which is the same as that presented by the Hessian matrix in the NR method. If none of the pixels is correlated, the Hessian matrix would be a diagonal matrix (Woo *et al* 1993). However, there are cross-correlations are among all pixels in EIT, which produce a skew form of an optimized matrix, in which the diagonal elements have the most significant values (see figure 1). Therefore, a similar approximation can also be made from the minimization function in equation (11) if $\bar{\boldsymbol{s}}^{\mathrm{T}}\bar{\boldsymbol{s}}$ approximates to a diagonal matrix (appendix A.3).

A physical definition follows the basic principle of the linear back-projection (LBP): the relative change in a boundary voltage measurement $\Delta V_j/V_j$ is linearly back-projected to each pixel between two equipotential lines in the case of the equipotential back-projection (Barber and Brown 1984), or over the whole domain in the case of the SBP (Kotre 1994) as a back-projection ratio. The sum of the products of the back-projection ratio and the weight factor/sensitivity coefficient at each pixel, normalized by the sum of their weight factors/sensitivity coefficients that are derived from all possible boundary measurements, approximately represents the relative change of the conductivity at this pixel.

Based on the LBP principle, Kotre (1994) produced the SBP algorithm as

$$\frac{\Delta\bar{\sigma}_k}{\sigma_0} \approx -\frac{\sum_{j=1}^{P} \frac{\Delta V_j}{V_j} \cdot s_{j,k}(\sigma_0)}{\sum_{j=1}^{P} s_{j,k}(\sigma_0)} \qquad (14)$$

where σ_0 is the measured or estimated conductivity for homogeneous distribution at the time of taking reference V.

Since conductivity is inversely related to voltage, a modified SBP algorithm (MSBP) based on the nonlinear

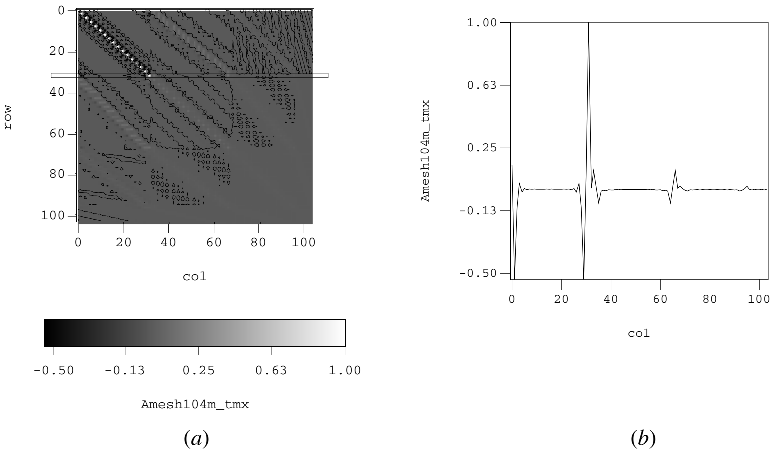

Figure 1. Normalized data distribution in the transformed 104 × 104 sensitivity matrix for use in the SCG method. (*a*) The value distribution in a grey level and contour plot, (*b*) a typical value distribution along the indicated row 36 in (*a*).

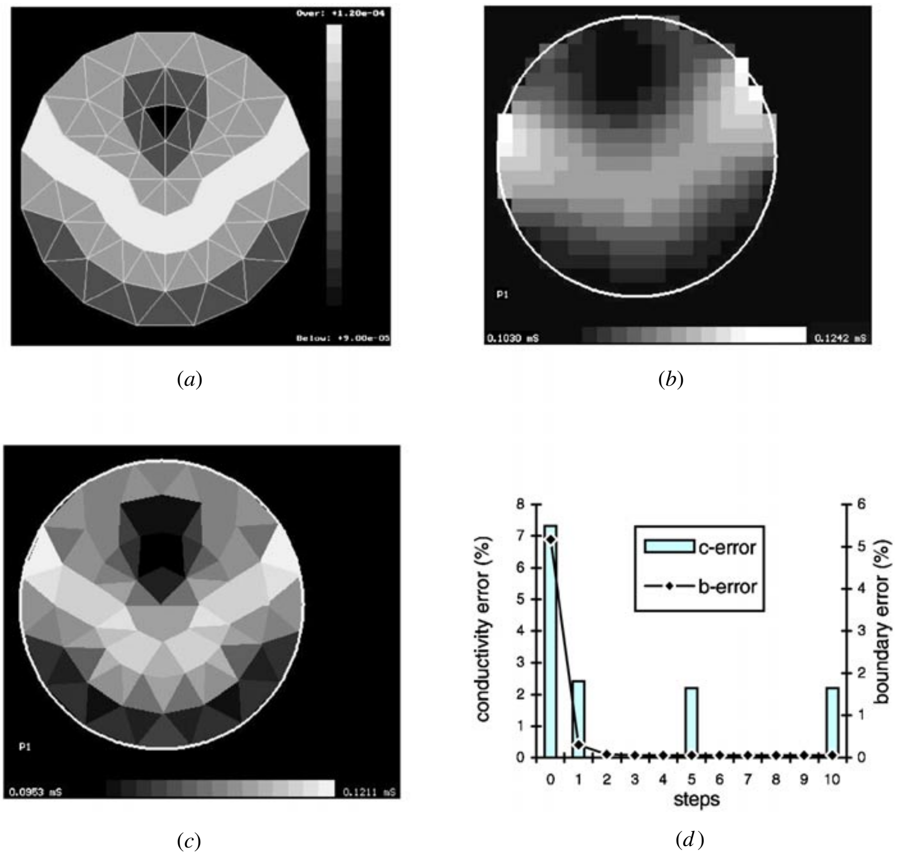

Figure 2. Reconstructed images from simulated data with small and general conductivity changes. (*a*) Conductivity set-up with four conductivity values, 0.09, 0.10, 0.11 and 0.12 mS cm^{-1}. (*b*) Image obtained from the MSBP. (*c*) Images obtained from the SCG with five solution steps and 20 iterations taken in the GCG for solving each inverse solution. (*d*) Convergence from reconstructing (*c*).

approximation, as given by equation (8), may extend the applicable range further (Wang *et al* 1996)

$$\bar{\sigma}_k = \sigma_0 + \Delta\bar{\sigma}_k = \sigma_0 \cdot \left(1 - \frac{\sum_{j=1}^{P} \frac{\Delta V_j}{V_j} \cdot s_{j,k}(\sigma_0)}{\sum_{j=1}^{P} s_{j,k}(\sigma_0)}\right) \approx \frac{\sigma_0 \cdot \sum_{j=1}^{P} s_{j,k}(\sigma_0)}{\sum_{j=1}^{P} \frac{V_j'}{V_j} \cdot s_{j,k}(\sigma_0)} \qquad (\Delta\bar{\sigma}_k \ll \sigma_0) \tag{15}$$

where $V_j' = V_j + \Delta V$ represents the measurement due to a conductivity change.

2.3. Electrode modelling

Image reconstruction algorithms are sensitive to small changes in the potential distribution. In order to avoid erroneous results, it is important to accurately model the size of the electrodes used in the physical phantoms or process vessels.

Results from simulations using analytical methods, such as the series expansion methods (SEM) and the conformal mapping technique, exhibit a similar profile to those acquired from a typical laboratory phantom (Pidcock 1994, Ider *et al* 1990). The FEM can be applied to model the shunting effects and contact impedance of the large electrodes (Cheng *et al* 1989, Hua *et al* 1993, Vauhkonen *et al* 1999).

In electrical impedance tomography, all electrodes are directly installed within the process vessels. There is no other material between the electrode and electrolyte inside the vessel. The effects of the double-layer capacitance (of the order of 10 μF cm^{-1} (Pollak 1974)), the charge transfer resistance (e.g. 500 Ω cm^2 at 13 mS cm^{-1} saline (Pollak 1974)) or the diffusion-layer impedance ($Z_d \propto f^{-0.5}$, e.g. $|Z_d| = 0.7\ \Omega$ cm at 100 Hz and 1×10^{-5} mol cm^{-3} NaCl (Cobbold 1974)) can be ignored for the frequency region (1 kHz to 200 kHz) most often used in many process tomography applications, especially when the sinusoidal current injection is adopted (Wang 1994).

The grouped node technique was employed (Wang *et al* 1995a, 1995b), via the FEM, to model the shunting effect of electrodes when a fine mesh is adopted in the FEM forward solution. However, for on-line measurement, the use of a coarse mesh can speed up the imaging speed. It is normally difficult to accurately simulate a physical electrode angle β (Wang *et al* 1995a, 1995b) when the FEM mesh has a limited number of boundary nodes. A reverse method for this case was suggested as equation (16) by estimating an effective electrode angle β of the 2D mesh, that is used for image reconstruction, and then using the electrode angle β for the design of the electrode system (Wang 1999):

$$\beta = \frac{2\pi N_d}{N_b + N_e} \tag{16}$$

where N_d is the number of nodes per electrode, N_b is the number of equispaced boundary nodes and N_e is the number of electrodes per sensing ring.

In the measurements presented in section 4, a fixed mesh with 224 elements and 32 boundary nodes is employed for image reconstruction, which gives an effective electrode angle of 0.13 rad. Based on the given electrode angle the electrode systems were designed with electrode angles of 0.133 and 0.135 rad for these applications with respect to the mixing vessel and test phantom. No contact impedance is added to the SCG image reconstruction in either the simulations or the applications reported here.

3. Simulation

To investigate the accuracy and the limitation of the multistep solution, a sequence of images were reconstructed and compared from simulated data. The set-ups were based on (a) a small conductivity change with point spread distribution, (b) a complex conductivity distribution, (c) a large conductivity difference, (d) two objects at positions that were difficult to distinguish. In addition, The antinoise capability of the SCG and the effect of the iteration number at each inverse step in the SCG were investigated. Only the adjacent sensing strategy (Brown and Segar 1985) was employed in these simulations. All references were taken from a homogeneous set-up with a conductivity of 0.11 mS cm^{-1}. A mesh with 104 triangular pixels was used for simulating all boundary voltages from these conductivity set-ups. All simulated data are in 32-bit precision format. To investigate the discretization error and the mesh adaptability used in the algorithm, some images were reconstructed using the mesh with 224 triangular pixels. Electrode positions in the 224-element mesh also had an anticlockwise rotation of 11.25° compared with those in the simulated set-ups using the mesh with 104 pixels in order to avoid the 'inverse crime'.

Considering the importance of the SBP in current applications, Some of the simulated data were also reconstructed using the MSBP (equation (15)), which may suggest the advantages and limitations of applying such an algorithm in industrial situations. A mesh with 316 square pixels was employed in the use of the MSBP algorithm. The electrode position at the square mesh has an 11.25° anticlockwise rotation compared with those in the simulated set-ups with the 104 triangular element mesh.

To assess the convergence rate of the SCG algorithm, an algorithm based on the NR method, named EIDORS (EIT and Diffuse Optical Tomography Reconstruction Software) (Vauhkonen *et al* 2000, UMIST 2000), was used to reconstruct some of these data. The linear approximation equations in the NR method are solved using Cholesky decomposition with Tikhonov regularization in each inverse step (Vauhkonen *et al* 1998). These images are reconstructed using a mesh with 492 elements. The parameters required for setting up EIDORS are the simulated contact impedance (0.005 Ω cm^{-1}), the Tikhonov regularization parameter (1×10^{-3} and 1×10^{-6} with respect to the relevant images) and the iteration number (6). The electrodes in the mesh for image reconstruction were positioned at a clockwise rotation of 11.25° compared with the simulation set-up mesh. The original simulated data were used for reconstructing images with the EIDORS. Considering that the results from EIDORS might be not comparable with those from SCG with 104 pixels due to the use of a different electrode model and a different number of mesh elements for computing the forward solution (boundary voltages), the SCG images were also reconstructed using the mesh with 224 triangular pixels and an 11.25° anticlockwise rotation. Further comparisons with real measurements are reported in the next section.

3.1. Small conductivity changes

For a set-up with small conductivity changes, both MSBP and SCG algorithms deliver relatively accurate results as demonstrated in figure 2. The SCG has shown a fast convergence speed for this set-up. The errors after the first step of the solution procedure are already 5.9 and 33% of the starting values, for boundary and conductivity errors respectively. The reconstructed conductivity error (RMS) is 2.2% after five steps with the SCG algorithm.

3.2. A complex conductivity distribution

A set-up with a complex conductivity distribution, as shown in figure 3(*a*), has been reconstructed as figures 3(*b*)–(*d*) using the MSBP, EIDORS (Tikhonov regularization parameter $= 1 \times 10^{-3}$) and SCG algorithms respectively. It is obvious that the MSBP approximation could not deliver an accurate

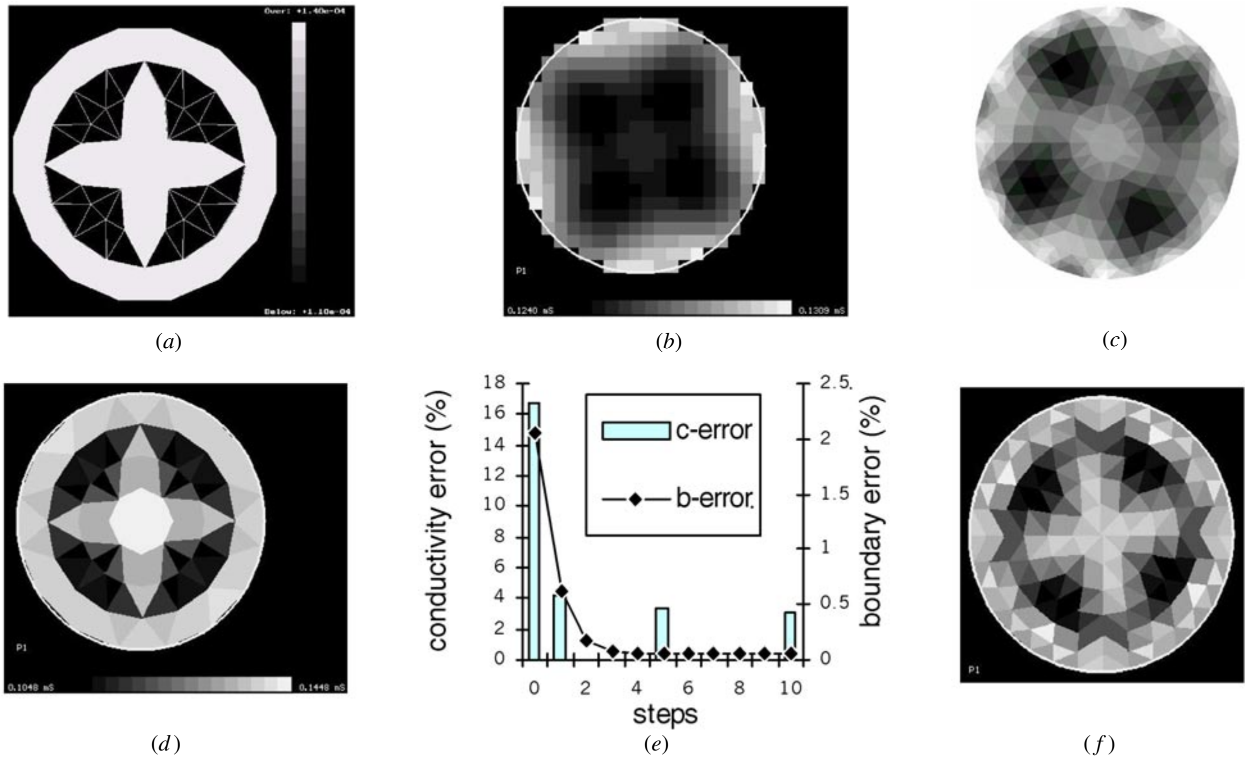

Figure 3. Reconstructed images from simulated data with a large difference in conductivity distribution. (*a*) Conductivity set-up with two conductivity values, 0.11 and 0.14 mS cm^{-1}. (*b*) Image obtained from the MSBP. (*c*) Image obtained from the EIDORS with six steps of solution (Tikhonov regularization parameter 1×10^{-3}). (*d*), (*f*) Image obtained from the SCG with five steps of solution and 20 iterations taken in the GCG for solving each inverse function. (*e*) Reconstruction convergence from (*d*).

image for this set-up (figure 3(*b*)). Both the EIDORS (figure 3(*c*)) and SCG (figures 3(*d*) and (*f*)) can reconstruct the complexity of the set-up. The image obtained from five steps of the SCG solution (figure 3(*d*)) has a conductivity error of 3.32% and a boundary voltage error of 0.055%. To observe the discretization error, a different mesh (224 elements) was employed and the reconstructed image can be seen in figure 3(*f*). The SCG presents a stable convergent image although its quality has been affected by the mesh discretization error.

3.3. A large conductivity difference

Figure 4 shows reconstructed results from a set-up with a large conductivity difference of 1:10. The image obtained from five steps of the inverse solution (SCG) gives a conductivity error of 14.3% and a boundary voltage error of 5.8% with a much sharper edge and smaller noise ripples across the background area (figure 4(*b*)). The boundary error was reduced linearly after three or more steps but there was little reduction in the conductivity error (figure 4(*c*)).

3.4. Imaging distinguishability

The imaging distinguishability of these algorithms was investigated and the results are given in figure 5. Two ‘objects’ are located along a radius of a mesh (figure 5(*a*)). For the set-up, the MSBP can be used to overview the presence of the two objects but could not distinguish them (figure 5(*b*)). The edge of the objects’ image is also merged with the boundary. The image obtained from EIDORS with the Tikhonov regularization parameter of 1×10^{-6} gives a better presentation of the location of the object (figure 5(*c*)). The images reconstructed with 20 steps of the SCG reveal a clear distinction between the two objects as well as their shape and size, although a certain artificial background noise is present (figures 5(*d*) and (*f*)).

In summary, all three algorithms can be used to reconstruct a small conductivity change with a point spread function distribution. The SCG has shown an advantage for reconstructing the set-ups with a complex conductivity distribution or a large conductivity difference. The EIDORS also has the capability of reconstructing these set-ups. However, the artificial effects can be identified from the blurred edges of the reconstructed images using EIDORS, which is probably introduced from the regularization for solving the linear equations based on an ill-conditioned Hessian matrix. The SBP is unable to reconstruct such set-ups. However, it can be used to extract the significance of these set-ups.

3.5. Antinoise capability

The antinoise capability of the SCG method was modelled and the results are given in figure 6. In these simulations, different noise levels are introduced into the simulated boundary voltages as shown in the top graphs of figure 6(*b*). The noise is generated at random with maximum relative changes of ±2.5 and ±5% respectively. The SCG with a fixed five-step inversion and 20 iterations for each GCG appears to have a

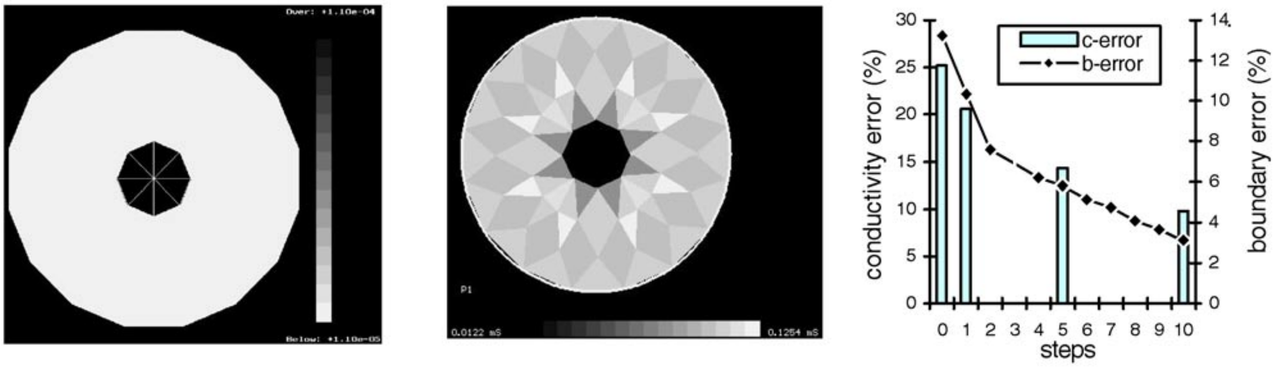

(*a*) (*b*) (*c*)

Figure 4. Reconstructed images from simulated data with large conductivity changes. (*a*) A conductivity set-up with two values, 0.011 and 0.11 mS cm^{-1}. (*b*) Image obtained from the SCG with five steps of solution and 20 iterations taken in the GCG for solving each inverse solution. (*c*) Reconstruction convergence from (*b*).

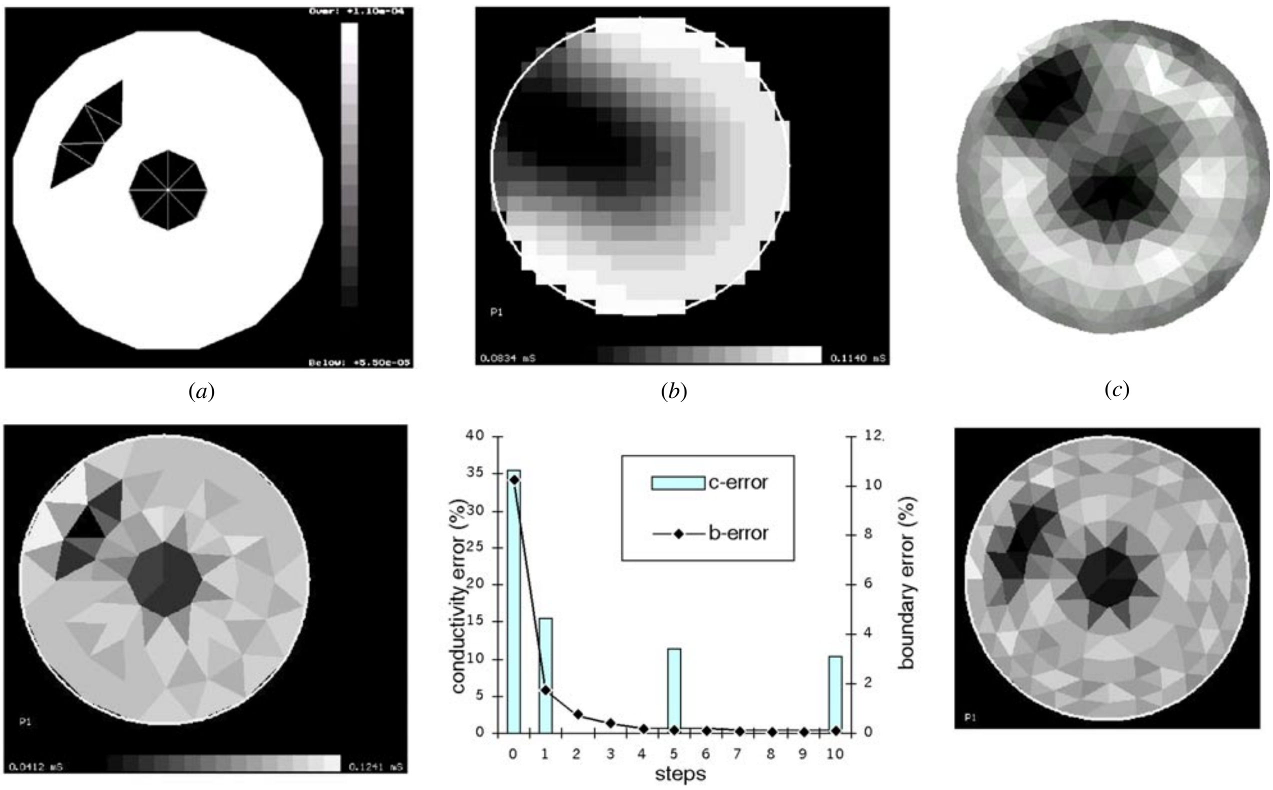

(*a*) (*b*) (*c*)

(*d*) (*e*) (*f*)

Figure 5. Reconstructed images for investigating imaging distiguishability. (*a*) Conductivity set-up with two conductivity values, 0.055 and 0.11 mS cm^{-1}. (*b*) Image obtained from the MSBP. (*c*) Image obtained from the EIDORS with six steps of solution (Tikhonov regularization parameter 1×10^{-6}). (*d*), (*f*) Image obtained from the SCG with 20 steps of solution and 20 iterations taken in the GCG for solving each inverse solution. (*e*) Reconstruction convergence from (*d*).

good antinoise capability when the noise level is less than ±2.5% (figures 6(*d*) and (*g*)). The MSBP demonstrates a high antinoise capability that allows it to extract the most significant (but not detailed) information from these noisy measurements (figures 6(*e*) and (*h*)). A similar approximation can also be made by applying a few iterations/steps to the SCG. The images in the right-hand column are reconstructed using SCG with five steps and two iterations for each GCG solution, which produce much clearer and more accurate images than those obtained from MSBP.

3.6. Effects of the iteration number

The effects of the iteration number taken in the GCG inverse step were also investigated by reconstructing the set-up shown in figure 5(*a*) with different iterations. Two sets of boundary voltage changes are employed. One was simulated using an FEM forward solution (called the 'true' boundary) and another was obtained by applying the conductivity set-up to equation (1) (called the 'linear' boundary). The reconstructed images with different numbers of iterations are given in figures 7(top) and 7(bottom) with respect to the

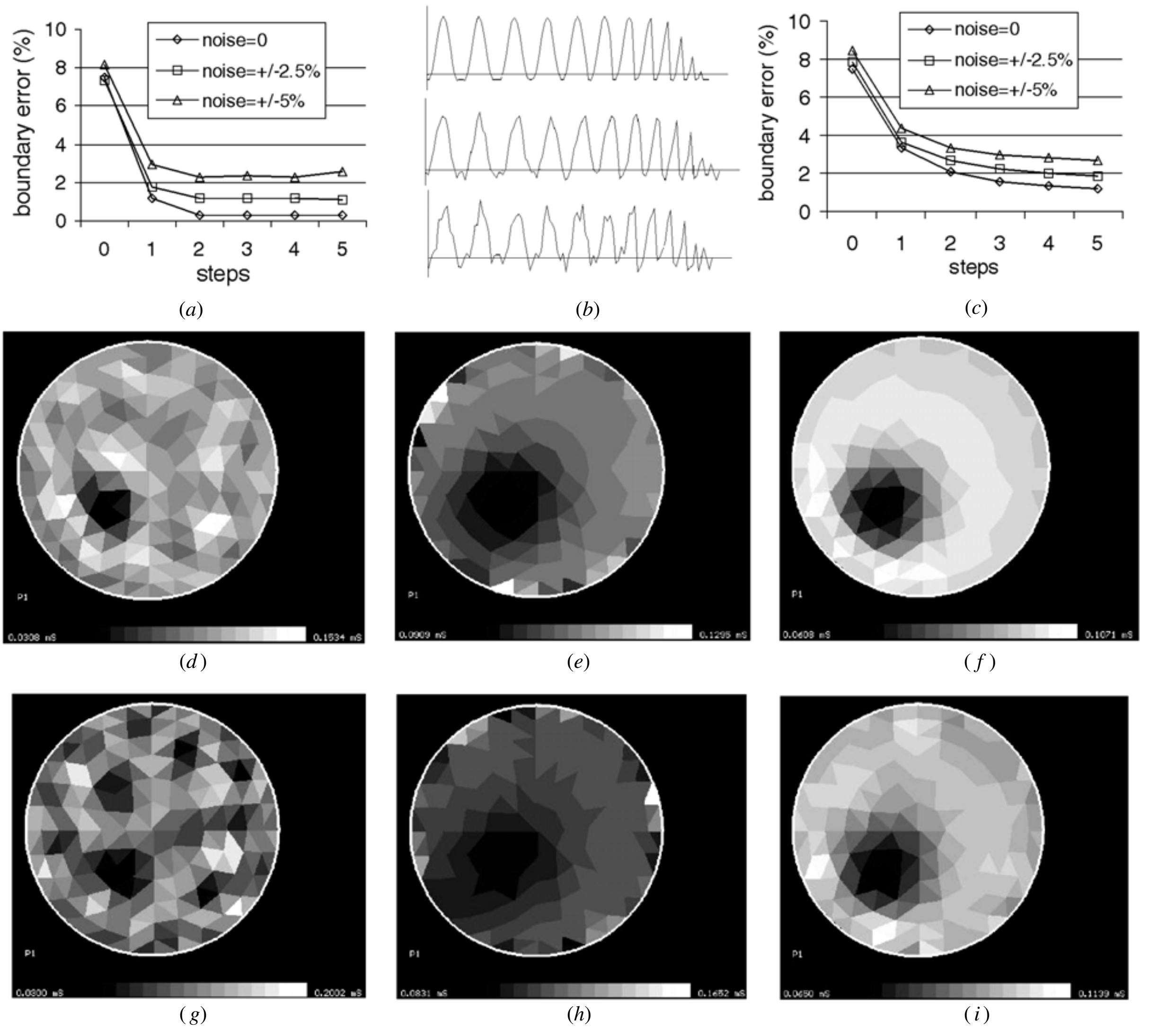

Figure 6. Reconstructed images from simulated data with random noise ±2.5% (*d*), (*e*), (*f*) and ±5% (*g*), (*h*), (*i*). The top graphs of (*b*) are examples of voltage relative changes with random noises 0, ±2.5 and ±5%. (*a*), (*c*) Convergence performances from reconstructing the images in its column. The images in the left and right columns are reconstructed using the SCG with five steps but 20 iterations (*d*), (*g*) and two iterations (*f*), (*i*) in each GCG step. The images in the middle column are reconstructed using MSBP.

'true' and 'linear' boundaries. The artificial noise increases in the image reconstructed with the 'true' boundary when the iteration number is higher than 50 (figure 7(top)). The images reconstructed using the 'linear' boundary, as given in figure 7(bottom), show an excellent convergence and demonstrate that a precise solution for equation (1) is possible if a linear relation exists even though an ill-conditioned sensitivity matrix is present. Two sets of convergence profiles are given in figure 8. The residuals of GCG from both boundary voltages are dropped quickly before iteration 10. The residuals are 8.7×10^{-5} and 4.8×10^{-5} at iteration 50, 2.7×10^{-5} and 1×10^{-5} at iteration 104, which demonstrates the solutions to equation (1) being reached from both boundary voltages. However, the boundary errors from both sets of data drop quickly before iteration 10. Afterwards, at high-order iterations, they increase from the 'true' boundary, but there is no change from the 'linear' boundary. The differences between the two boundary voltages are plotted in figure 9, which demonstrates that significant errors may arise due to the assumption of linearity for equation (1). It is obvious that the disconvergence at the high iteration in figure 7(top) is caused by the assumption of linearity and the areas most affected at the high iteration are located at the pixels with low sensitivity or small eigenvalues. The iteration number in the GCG method plays a similar role to the regularization factor used in general regularization methods, such as the Marquardt method or the Tikhonov method, which results in an approximate solution at each step. Comparing the images (figure 10(*a*)) reconstructed using the NR algorithm with the Cholesky decomposition and Tikhonov regularization, those images (figure 10(*b*)) reconstructed using SCG algorithm with the GCG method appear to more precisely approach the true value.

This phenomenon suggests that accurately solving equation (1) could produce a conductivity distribution with a significant artificial error, particularly for a large relative change in conductivity. The approximate solution for equation (1) plays an important role in the nonlinear inverse solution although the ill-conditioned sensitivity matrix is

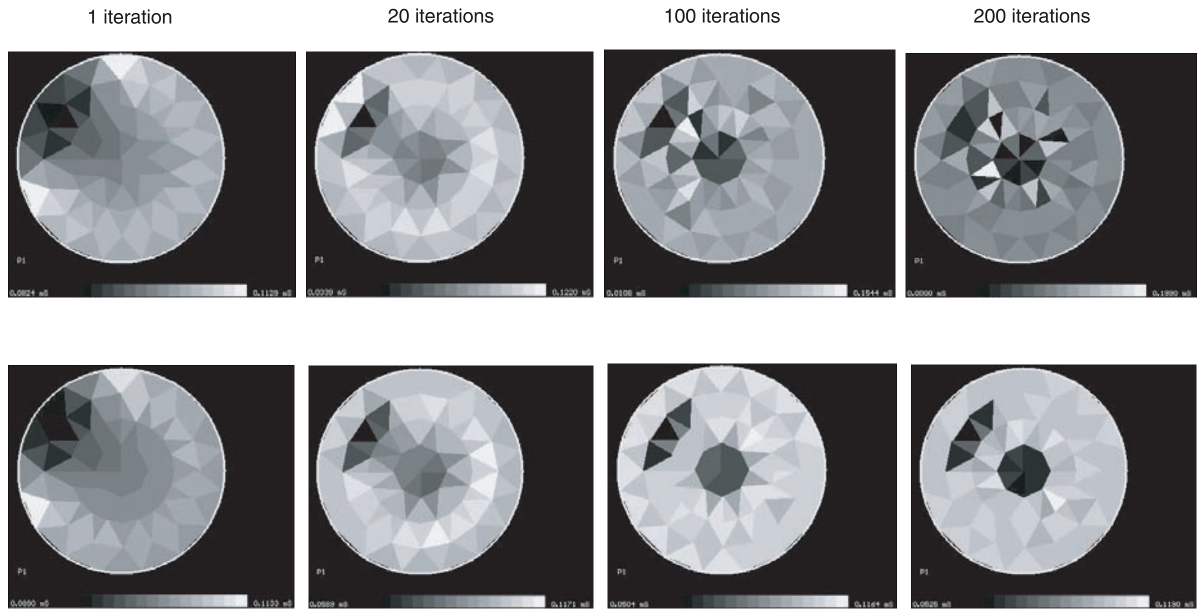

Figure 7. Artificial error caused by the linear approximation (images are reconstructed using the GCG with the indicated iterations). Top images are reconstructed from the 'true' boundary voltages simulated with the FEM method. Bottom images are reconstructed from the 'linear' boundary voltages produced with the linear approximation equation (1).

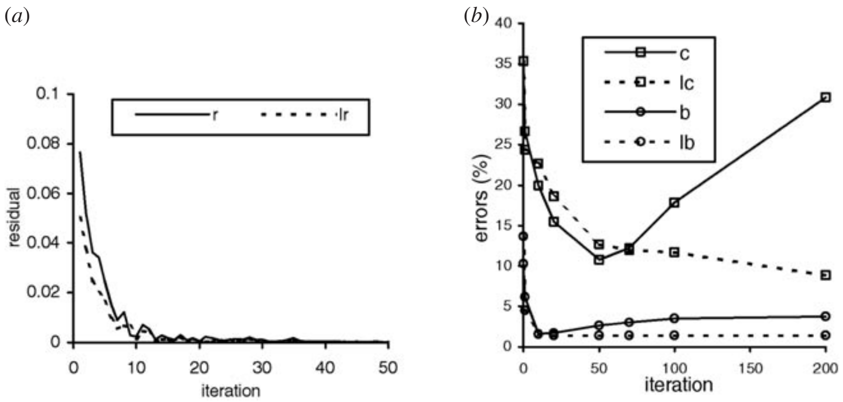

Figure 8. Convergence from reconstructing images in figure 7. (*a*) RMS value of the GCG residual. (*b*) Conductivity and boundary errors. The full curves are in respect to the 'true boundary' voltage and the dotted curve in respect to the 'linear boundary' voltages (c denotes conductivity error, b denotes boundary error and r denotes residual).

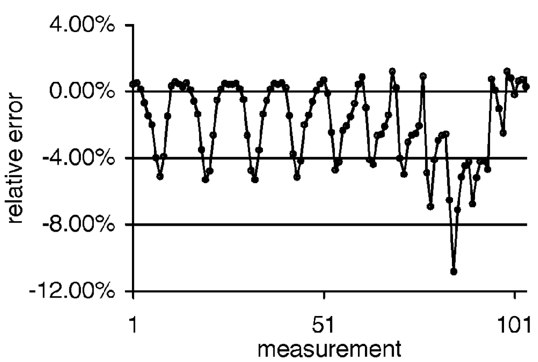

Figure 9. Relative errors between the linear boundary voltages and the true boundary voltage.

another matter. Therefore, choosing the right iteration number in the SCG will result in a faster convergence speed and better image quality. In general, the choice can be estimated according to the size of the relative change in conductivity, voltage or measurement noise.

3.7. *Effects of the inverse steps*

Incrementing the number of steps required for solving the nonlinear problem may improve imaging accuracy (figure 11). However, the most significant contribution is from the first step, which has already been shown in previous convergence graphs. In practice, due to the high level of noise in the measurement signal, the use of a high-order step could lead to a noisy image (figure 6(*g*)). A single solution using a precalculated sensitivity matrix without the involvement of a forward solution would be widely acceptable for the balance of imaging accuracy and speed. As an example, some images (figure 12) have been reconstructed with the single-step solution using data from the previously discussed set-ups.

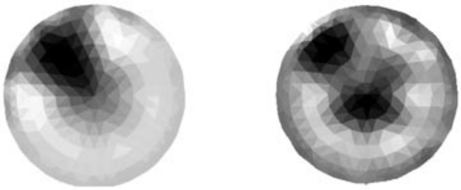

TR = 1×10^{-3} TR = 1×10^{-6}

(*a*)

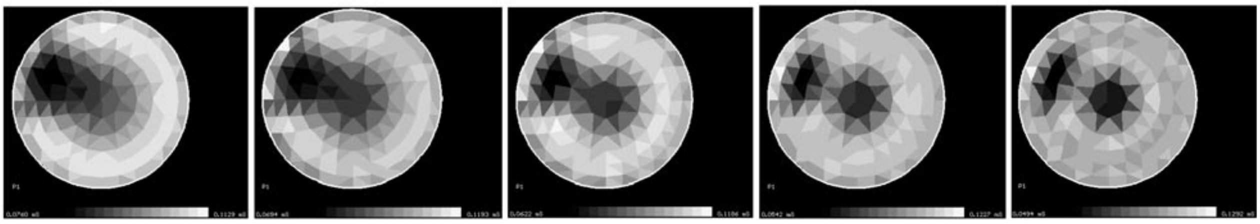

its = 1 its = 2 its = 5 its = 10 its = 20

(*b*)

Figure 10. Effects of regularization in the multistep inverse solution. (*a*) Reconstruction with the six-step NR method/Choleskey decomposition with different Tikhonov regularization factors (EIDORS). (*b*) Reconstruction with the five-step SCG method/GCG with different iterations.

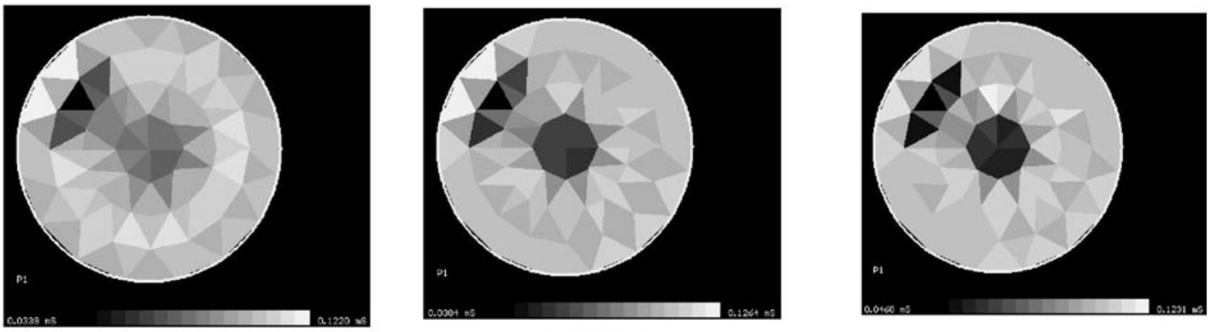

single step 10 steps 40 steps

Figure 11. Effects of different steps in the use of the SCG (20 iterations taken in the GCG for solving the inverse solution in each step).

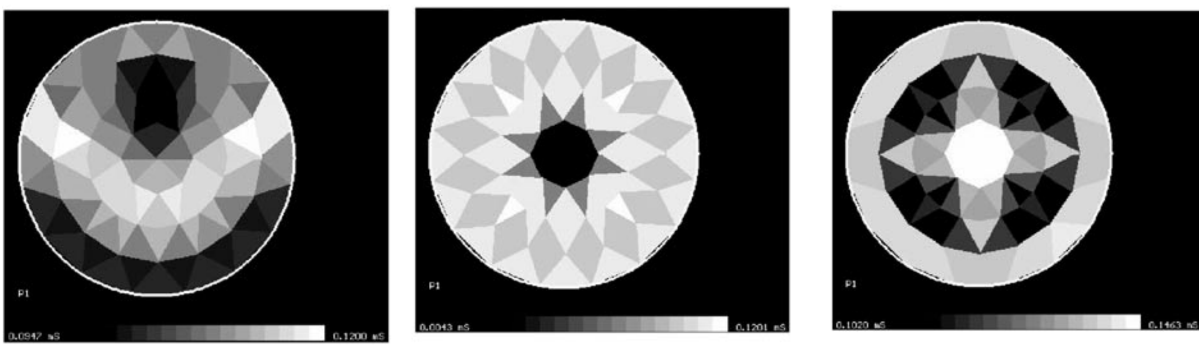

Figure 12. Images reconstructed using the single-step solution with 20 iterations taken in the GCG method.

3.8. Running time

Reconstruction timings were tested using a PC with a 350 MHz Pentium II processor. The program and associated algorithm libraries (Sparse matrix generator, CG and GCG methods for forward and inverse solutions, Sensitivity matrix generation, etc) were written using C^{++}. Results are shown in table 1. Using a precalculated sensitivity matrix, the MSBP method gives a fixed reconstruction time based on the number of reconstructed mesh elements, which is almost linear in the increment of mesh elements. The speed of SCG is much slower than that of MSBP, which is the product of the solution steps and the sum of the time taken for the forward solution, the inverse solution and some overheads. The solution timings given in table 1 are only in regard to one iteration taken in the GCG inverse step.

Table 1. Reconstruction timings.

Reconstruction method	Number of elements on mesh	Forward solution (ms)	Inverse solution/ iteration step (ms)
MSBP	104		6.04
	224		12.6
	316		18.1
SCG	104	190	17.8
	224	575	38.5

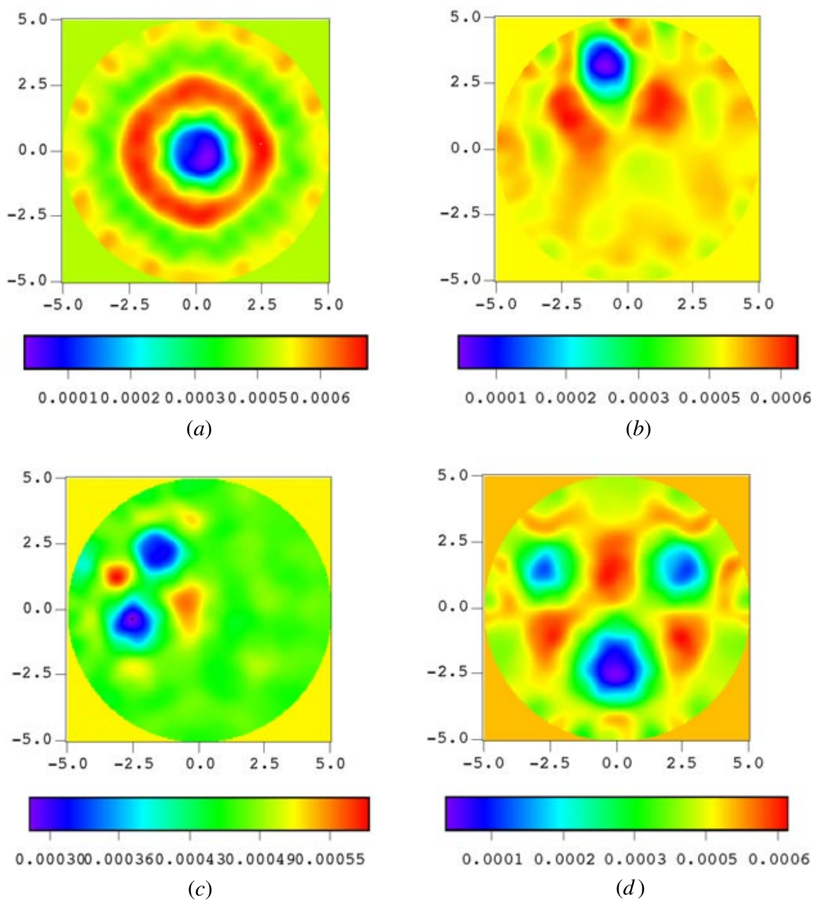

Figure 13. Reconstructed images from a test phantom: (*a*) and (*b*) a 2.5 cm glass bar, (*c*) two 2.5 cm glass bars, (*d*) three glass bars of diameters 2, 2.5 and 4 cm.

4. Measurement

4.1. Imaging capability verification from a testing phantom

A sequence of tests were performed using a 14.8 cm diameter Perspex vessel mounted with a ring of 16 1×3 cm^2 electrodes and filled with 0.473 mS cm^{-1} brine. The adjacent electrode sensing strategy was employed with a pair of 5 mA sinusoidal currents at 9.6 kHz. Images were reconstructed using the SCG algorithms with five iterative steps. The first experiment was designed to investigate the imaging sensitivity across the radius of the vessel. Data were collected when a 2.5 cm diameter glass bar was moved from the centre to the periphery of the vessel. Two of these images, of the bar positioned at the centre and the side of the phantom, are given in figures 13(*a*) and (*b*). The reconstructed objects have shown a similar conductivity value (both less than 0.1 mS cm^{-1}) and geometrical size at both imaging positions. Background ripple noise produced from the SCG can also be observed. The second experiment used two glass bars with the same diameter (2.5 cm) and the third used three glass bars with different diameters (2.0, 2.5 and 4 cm). Their images were reconstructed and are given in figures 13(*c*) and (*d*), The two objects in figure 13(*c*) and the size of the three glass bars in figure 13(*d*) can each be clearly distinguished and measured.

4.2. Imaging gas–liquid mixing in a pilot plant

EIT has been shown to be useful in detecting mixing conditions inside a stirred vessel caused by the mixing reaction, different impeller types and malfunction (Holden *et al* 1998). A mixing vessel of diameter 1.5 m was used, which was equipped with eight planes of 16-electrode rings and fitted with a Rushton turbine impeller (one-third of the vessel diameter) in a standard configuration with four equispaced wall-mounted baffles. Air

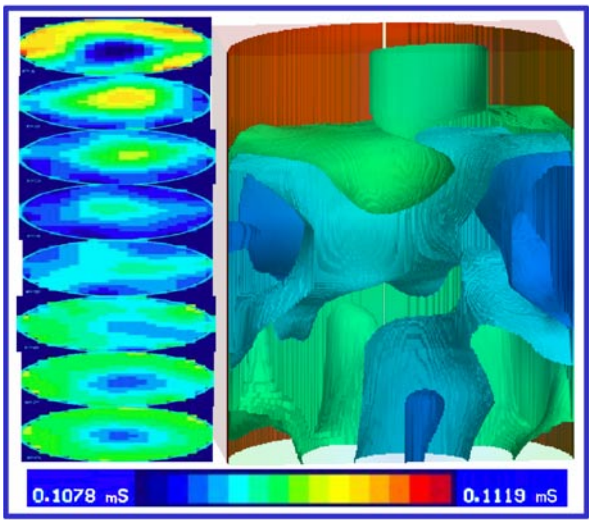

(*a*)

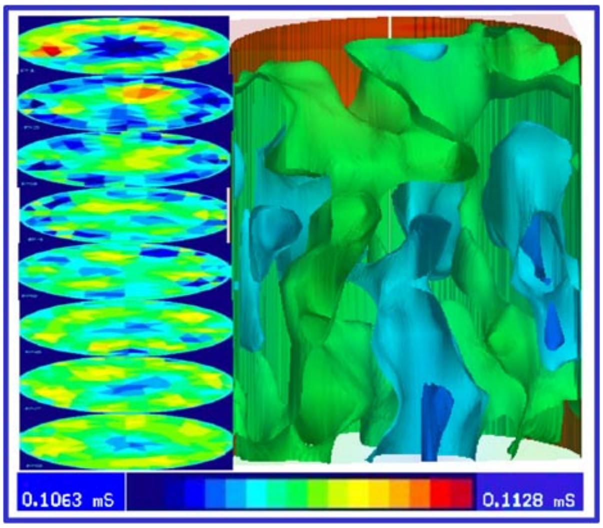

(*b*)

Figure 14. Gas hold-up images from a gas–liquid mixing (water conductivity 0.11 mS cm^{-1}). The slice images in (*a*) and (*b*) are raw images reconstructed with the MSBP and SCG algorithms with which the 3D images in the right of (*a*) and (*b*) are interpolated. Three concentration regions are isosurfaced with 0.109 82, 0.109 20 and 0.108 80 mS cm^{-1} for the MSBP image and 0.109 88, 0.108 72 and 0.108 03 mS cm^{-1} for the SCG image (interpolated using Spyglass v1.00).

was fed into the vessel along a pipe and injected upwards directly below the centre of the disc turbine. Eight two-dimensional (2D) slice tomograms of an instant gas hold-up in the mixing vessel were reconstructed using the MSBP and the single-step SCG. A three-dimensional (3D) image of the gas hold-up can be interpolated from eight 2D images reconstructed with MSBP and SCG in figures 14(*a*) and (*b*) respectively. A similar overall distribution of gas concentration is reflected in both images, although particular features exist in each image. Validation of such dynamic tomographic imaging is still a topic of dispute. Relevant information can be found in Williams and Beck (1995) and Mavros (2001).

4.3. Imaging a human hand

In another interesting test, a human hand was scanned using an EIT system. A 14.8 cm diameter vessel fitted with one 16-electrode ring sensor and filled with 5.16 mS cm^{-1} brine was used. The adjacent electrode sensing strategy was applied with a pair of 10 mA sinusoidal currents at 9.6 kHz for the test. The image data comprised 15 measurement data sets acquired as the hand moved along the axial direction of the phantom while the volume of water was kept the same. The signal-to-noise-ratio (SNR, here the repeatability of the reference voltage) was checked, which was within a maximum error of 0.5% at the start and 2.5% at the end of the scanning. Fifteen 2D images were reconstructed with the SCG algorithm with three steps of the inverse solution, given in figure 15.

According to general knowledge about the conductivity of a human arm, most parts that make up the arm have a conductivity of less than 5.0 mS cm^{-1} (arm, longitudinal 4.2 mS cm^{-1}; arm, transverse 1.58 mS cm^{-1}; muscle, average 1.89 mS cm^{-1}; bone 0.0625 mS cm^{-1}, fat 0.4 mS cm^{-1}) (Barber and Brown 1984). It is obvious that the highest and lowest conductivity in the reconstructed conductivity distribution is not reliable; this could be caused by signal noise from the measurements, by artificial errors, by the assumption of linearity in the sensitivity theorem and the 2D approach of the SCG algorithm. Nevertheless, some details of the properties of the hand can be identified from these images, such as a high-conductive muscle region (in slices 1, 2), a low-conductive bone region (in slices 1, 2, 3, 4), a skin region (in slice 1) and finger regions (in slices 7–13). The quantitative values presented in each image slice can be used to extract the surface of a similar region eliminating the effects of these noises. A cutting value of 3.3 mS cm^{-1} is applied to extract the surface of the skin of the hand as an isosurface using Spyglass v1.00. An outline of the human hand has been successfully extracted as shown in figure 16. Some distortions can also be found, which may be caused by electrode noise, the unstable position of the hand during scanning and the 3D effect of the electrical field.

4.4. Imaging comparison

In order to avoid the problem of divergence caused by the measurement noise and the electrode modelling error, the measurement data for the use of EIDORS were transformed by applying the products of their relative changes and the reference voltages from the forward solution of EIDORS, which are the same processes as those in MSBP and SCG. This transform provides an equal platform for comparisons between the three algorithms. Two sets of measurements from the experiment described in section 4.3 were used to demonstrate the imaging capabilities. Figures 17(*a*)–(*f*) show the first and ninth slice images of the human hand, which were reconstructed with the MSBP, EIDORS and SCG algorithms, respectively. The high-conductive muscle range, the low-conductive skin on the edges of the wrist part and the five fingers can be visualized from the images reconstructed with the SCG. The EIDORS appears to have a better capability than the MSBP, but the images are less detailed than those of

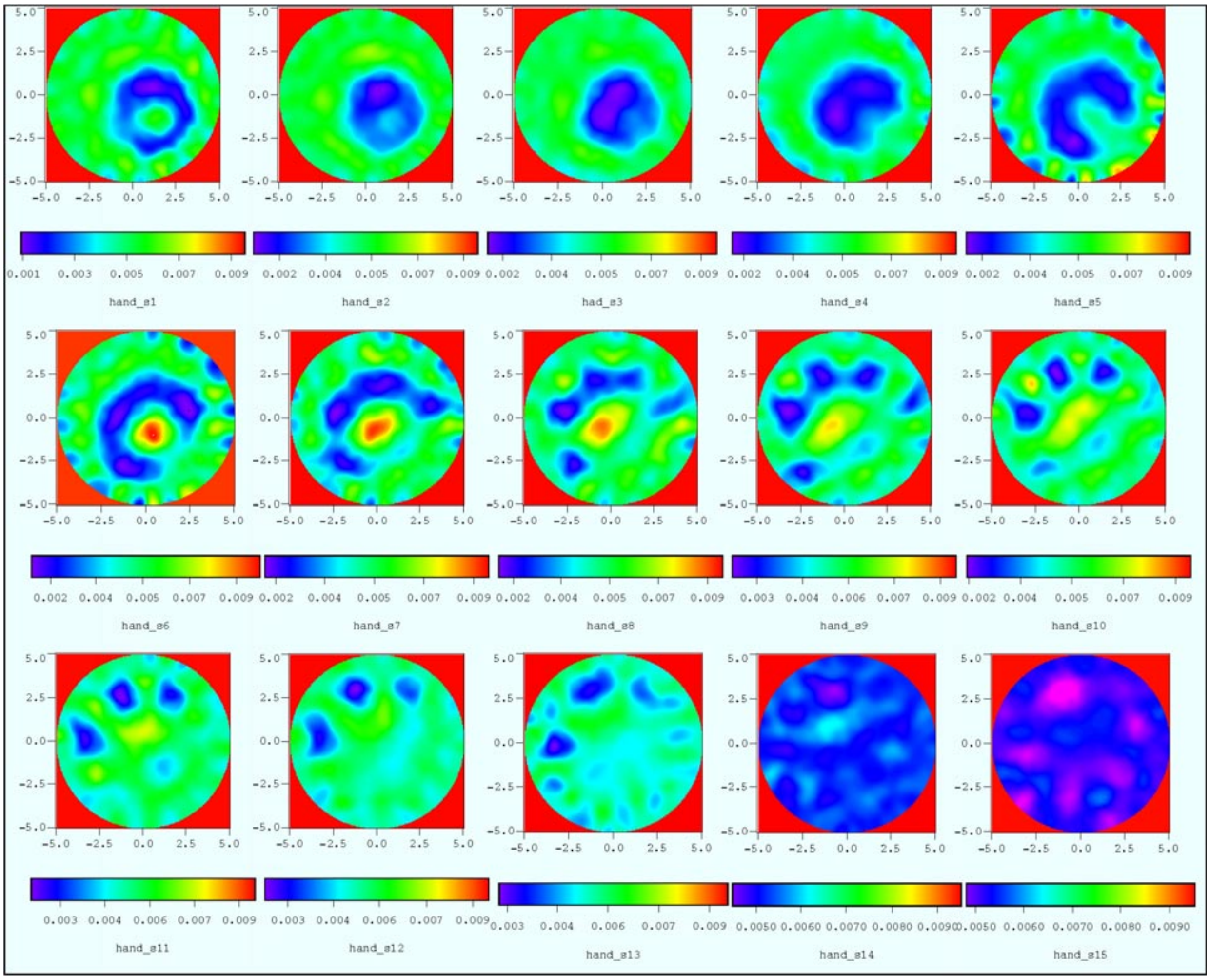

Figure 15. Slice images of a human hand in 0.516 mS cm^{-1} brine scanned with an EIT system (in the order from left to right and top to bottom going from the wrist to the fingers). Images are reconstructed using the SCG with three steps of inversion and then linearly smoothed with Spyglass v1.01.

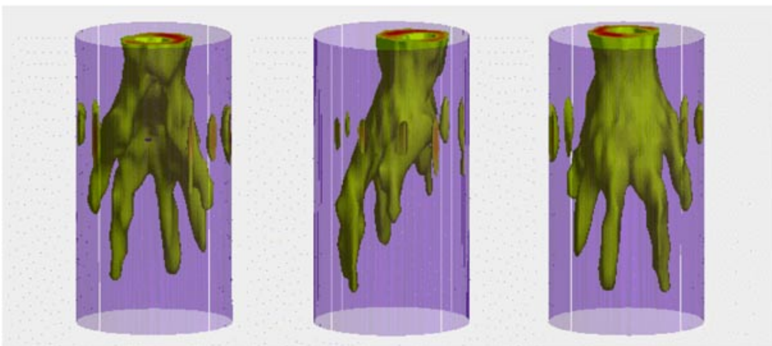

Figure 16. 3D hand images interpolated from the 2D EIT images given in figure 15 and then isosurfaced with a cutting value of 3.3 mS cm^{-1} (Spyglass v1.01).

the SCG. The effect of regularization used in EIDORS can be observed; it blurs the image details and produces a much more homogeneous background. The MSBP can only outline the overall information.

5. Conclusions

A sensitivity theorem based inverse solution using generalized conjugate gradients methods (SCG) with a method of error vector decomposition has been developed. This method employs a multistep approach with the sensitivity theorem based linear approximation and uses the differences between the relative changes in the measured and simulated voltage at each step to solve inverse problem of the nonlinear electric field.

The precise solution of the inverse problem, whether in the direct method or the indirect method, using the linear

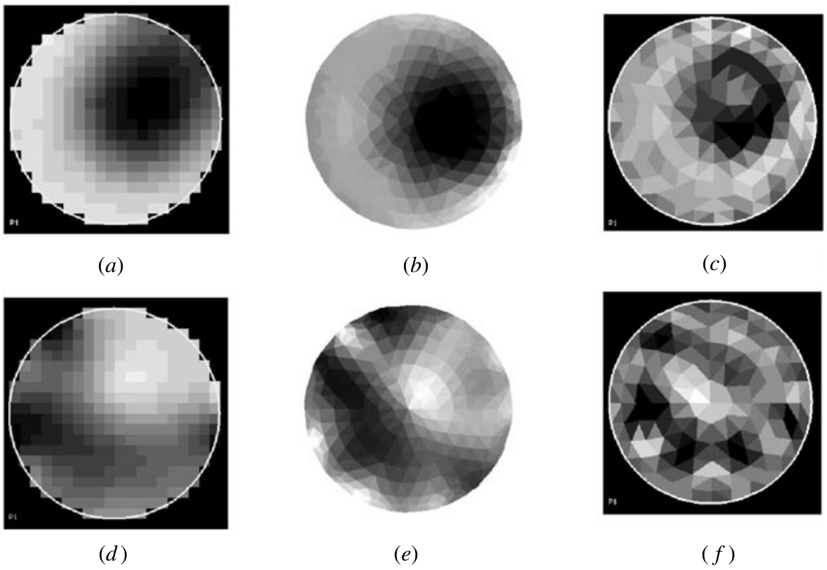

Figure 17. The 1st and 9th slice images of a human hand ((*a*)–(*c*), (*d*)–(*f*) respectively). The images in the left-hand column were reconstructed with MSBP. The images in the middle column were reconstructed using EIDORS with regularized data. The images in the right-hand column were reconstructed with SCG.

approximation can produce a conductivity distribution with significant artificial errors; these are caused by both the use of the linear assumption and the ill-conditioned sensitivity matrix. In general, regularization methods such as the Marquardt and the Tikhonov regularization methods have to be applied to obtain an approximate solution at each inverse step. This method of regularization may introduce additional artificial errors. In the use of the GCG method, approximation at each inverse step is controlled by the number of iterations without applying additional regularization factors. The choice of the number of iterations for the GCG inverse solution at each step can affect the ratio of convergence, as well as the imaging precision. The number of iterations taken in the GCG inversion can be estimated according to the size of the relative changes in conductivity or voltage as well as the measurement noise. The use of the error function decomposition method in SCG solution can greatly reduce the effects of electrode modelling errors, minimize the instrumental errors, subtract the background and therefore highlight the low contrast change in the region of interest. The algorithm has demonstrated its apparent advantages in its precision, reconstruction convergence and antinoise capability. A single-step SCG solution could be widely acceptable for the balance of imaging accuracy and executable speed of the algorithm considering the achievable signal-to-noise ratio in industrial applications. Compared with direct inverse solutions utilizing some regularization techniques, the conjugate gradients method is more attractive, since the GCG solution gives an easily controlled residual vector instead of a precise solution.

Since the SCG solution is based on a linear approximation for each Step, an ill-conditioned sensitivity matrix and a limited number of boundary measurements, it produces an approximate solution, particularly for large conductivity differences. Artificial errors may be introduced into the solution due to an incomplete modelling of the electric field when computed reference voltages have to be used in the SCG solution. It should also be noted that the resultant images present a conductivity distribution in relation to that at the time of taking the references. The effect of the subtraction should be taken into account for the implementation of the SCG image if an inhomogeneous conductivity distribution is present at the time of taking the references. Although 3D measurement patterns can be transformed to 2D patterns to adapt a 2D algorithm, the error caused by the 3D effect of the electric field still exists (Wang 1999). The modified sensitivity back-projection algorithm (MSBP) has apparent advantages in its simplicity, fast speed of operation and antinoise capability, but it has a very limited achievable accuracy.

Acknowledgments

The author would like to thank Dr W Yin, Dr N T Holliday and Mrs N Liu for their assistance in the preparation of this paper.

Appendix

A.1. Sensitivity theorem

The lead theorem was derived from the divergence theorem (A.1) by Geselowitz (1971) and Lehr (1972) for impedance plethysmography. The mutual impedance change ΔZ for a four-electrode system, derived by Geselowitz and Lehr and later linearized by Murai and Kagawa, is given as (A.2) and (A.3) respectively, where ψ and ϕ are potential distributions in response to the presence of currents I_ψ and I_ϕ at two ports (A–B and C–D) respectively

$$\int_\Omega \nabla \cdot \boldsymbol{A}\,\mathrm{d}\Omega = \oint_S \boldsymbol{A} \cdot \mathrm{d}S \tag{A.1}$$

where Ω is a region bounded by a closed surface S, $\boldsymbol{A}$ is a vector function of the position

$$\Delta Z = \frac{\Delta\phi_{AB}}{I_\phi} = \frac{\Delta\psi_{CD}}{I_\psi} = -\int_\Omega \Delta\sigma \frac{\nabla\phi^{\Xi}}{I_\phi} \cdot \frac{\nabla\psi}{I_\psi}\,\mathrm{d}\Omega \tag{A.2}$$

where ϕ^{Ξ} is the potential change caused by a change of conductivity $\sigma^{\Xi} = \sigma + \Delta\sigma$

$$\Delta Z = -\int_{\Omega} \Delta\sigma \frac{\nabla\phi}{I_\phi} \cdot \frac{\nabla\psi}{I_\psi} \,\mathrm{d}\Omega + 0((\Delta\sigma)^2)$$
$$\approx -\int_{\Omega} \Delta\sigma \frac{\nabla\phi}{I_\phi} \cdot \frac{\nabla\psi}{I_\psi} \,\mathrm{d}\Omega \qquad (\Delta\sigma_k \ll \sigma_k). \tag{A.3}$$

The mutual impedance Z of the four-electrode system for a known conductivity distribution can be derived by substituting $\psi\boldsymbol{J}_\phi$ or $\phi\boldsymbol{J}_\psi$ into the divergence theorem (A.1) and then substituting $\boldsymbol{J}_\phi = -\sigma_\phi\nabla\phi$ or $\boldsymbol{J}_\psi = -\sigma_\psi\nabla\psi$ into the left-hand side of the resulting expression under the condition of no internal current source (Wang 1995a):

$$Z = \frac{\phi_{AB}}{I_\phi} = \frac{\psi_{CD}}{I_\psi} = \int_{\Omega} \sigma \frac{\nabla\phi}{I_\phi} \cdot \frac{\nabla\psi}{I_\psi} \,\mathrm{d}\Omega. \tag{A.4}$$

Supposing that the conductivity distribution is composed of w small uniform 'patches' or pixels, then (A.3) and (A.4) can be expressed as (A.5) and (A.6) and the sensitivity coefficient s for each discrete pixel is given by (A.7) (Murai and Kagawa 1985, Breckon and Pidcock 1987, Barber 1990), where Ω_k stands for a discrete 2D area at location k

$$\Delta Z = \sum_{k=1}^{w} \Delta\sigma_k S_{\phi,\psi,k} \tag{A.5}$$

$$Z = -\sum_{k=1}^{w} \sigma_k S_{\phi,\psi,k} \tag{A.6}$$

$$s_{\phi,\psi,k}(\sigma_k) = -\int_{\Omega_k} \frac{\nabla\phi}{I_\phi} \cdot \frac{\nabla\psi}{I_\psi} \,\mathrm{d}\Omega_k. \tag{A.7}$$

A.2. Conjugate gradients methods

Conjugate gradients (CG) methods provide a quite general means of solving the $N \times N$ linear system as given by (A.8) (Press *et al* 1992). The ordinary CG algorithm is only applicable in the case that $\boldsymbol{A}$ is symmetric and positively defined (Golub and Van Loan 1989). It is based on the idea of minimizing the function (A.9) to give a *gradient* or residual function as (A.10) that is equivalent to (A.8) when the *gradient* or residual is zero

$$\boldsymbol{A} \cdot \boldsymbol{x} = \boldsymbol{b} \tag{A.8}$$

$$f(x) = \tfrac{1}{2}\boldsymbol{x} \cdot \boldsymbol{A} \cdot \boldsymbol{x} - \boldsymbol{b} \cdot \boldsymbol{x} \tag{A.9}$$

$$\nabla f = \boldsymbol{A} \cdot \boldsymbol{x} - \boldsymbol{b} \qquad \text{or} \qquad \boldsymbol{r} = \boldsymbol{A} \cdot \boldsymbol{x} - \boldsymbol{b}. \tag{A.10}$$

The minimization is carried out by generating a succession of search directions of vectors $\boldsymbol{p}_k$, which represent, as nearly as possible, the directions of the improved minimizers $\boldsymbol{x}_k$. The term *conjugate* means that the vectors are orthogonal with respect to $\boldsymbol{A}$ and hence satisfy the condition (Jennings and McKeown 1992)

$$\boldsymbol{p}_i^{\mathrm{T}} \boldsymbol{A} \boldsymbol{p}_j = 0 \qquad \text{for} \quad i \neq j. \tag{A.11}$$

The solution may be accomplished by the following procedures:

(1) Approximate an initial solution vector and calculate the initial residual and direction vectors $\boldsymbol{r}_0$, $\boldsymbol{p}_0$

$$\boldsymbol{x}_0 = (x_1^{(0)}, x_2^{(0)}, \ldots, x_N^{(0)})^{\mathrm{T}} \qquad \boldsymbol{p}_0 = \boldsymbol{r}_0 = \boldsymbol{b} - \boldsymbol{A}\boldsymbol{x}_0.$$

(2) Carry out the iterations below from $k = 0$ to $N - 1$, until the residual $\boldsymbol{r}_k$ is sufficiently small

$$\begin{aligned} \boldsymbol{u}_k &= \boldsymbol{A}\boldsymbol{p}_k \\ \alpha_k &= \boldsymbol{r}_k^{\mathrm{T}}\boldsymbol{r}_k / \boldsymbol{p}_k^{\mathrm{T}}\boldsymbol{u}_k \\ \boldsymbol{x}_{k+1} &= \boldsymbol{x}_k + \alpha_k \boldsymbol{p}_k \\ \boldsymbol{r}_{k+1} &= \boldsymbol{r}_k - \alpha_k \boldsymbol{u}_k \\ \beta_k &= \boldsymbol{r}_{k+1}^{\mathrm{T}}\boldsymbol{r}_{k+1} / \boldsymbol{r}_k^{\mathrm{T}}\boldsymbol{r}_k \\ \boldsymbol{p}_{k+1} &= \boldsymbol{r}_{k+1} - \beta_k \boldsymbol{p}_k. \end{aligned} \tag{A.12}$$

In the case when the coefficient matrix $\boldsymbol{A}$ is indefinitely symmetric, the generalized conjugate gradients (GCG) formulations can be applied using the method of the minimum residuals or the method of biconjugate gradients without increasing the singularity of $\boldsymbol{A}$ (Jennings and McKeown 1992, Press *et al* 1992). For solving a large system of sparse equations, its convergence characteristics were found to make it one of the best iterative methods (Reid 1971), particularly for a matrix with optimized data distribution (the most significant values at and attenuated from the diagonal elements), but more vector operations and stores are required (Jennings and McKeown 1992).

A.3. Diagonal matrix approximation

For a linear equation (A.8), the minimization function (A.14) can be obtained from minimizing (A.13)

$$f(\boldsymbol{x}) = \tfrac{1}{2}\|\boldsymbol{A}\boldsymbol{x} - \boldsymbol{b}|^2 \tag{A.13}$$

$$\nabla f(\boldsymbol{x}) = \boldsymbol{A}^T(\boldsymbol{A}\boldsymbol{x} - \boldsymbol{b}) \tag{A.14}$$

where $\boldsymbol{r}$ is a residual vector. Let $\nabla f = 0$, then the solution can be made to (A.15) if an inverse matrix of $\boldsymbol{A}^{\mathrm{T}}\boldsymbol{A}$ exists

$$\boldsymbol{x} = (\boldsymbol{A}^T\boldsymbol{A})^{-1}\boldsymbol{A}^T\boldsymbol{b}. \tag{A.15}$$

For a particular example, the solution is approximate to (A.16), if the $\boldsymbol{A}^{\mathrm{T}}\boldsymbol{A}$ can be approximated as a diagonal matrix

$$\boldsymbol{x} \approx \tau\boldsymbol{A}^T\boldsymbol{A}\boldsymbol{x} = \tau\boldsymbol{A}^T\boldsymbol{b} \tag{A.16}$$

where τ is the inversed matrix for the approximated diagonal matrix of $\boldsymbol{A}^{\mathrm{T}}\boldsymbol{A}(\boldsymbol{A} = [a_{ij}])$, in which its diagonal parameters satisfy

$$\tau_{jj} = \frac{1}{\sum_i^N (a_{ij})^2}. \tag{A.17}$$

The error function is

$$\boldsymbol{r} = \tau\boldsymbol{A}^T\boldsymbol{A}\boldsymbol{x} - \tau\boldsymbol{A}^T\boldsymbol{b} \tag{A.18}$$

where $\boldsymbol{r}$ is a residual vector. An iterative solution can be obtained in a kind of the Landweber iteration method as (Landweber 1951)

$$\boldsymbol{x}_n \approx \boldsymbol{x}_{n-1} - \boldsymbol{r}_n = \boldsymbol{x}_{n-1} - \tau\boldsymbol{A}^T(\boldsymbol{A}\boldsymbol{x}_{n-1} - \boldsymbol{b}). \tag{A.18}$$

The selection of τ for the SBP has been discussed in section 2.3 of this paper. An example for capacitance tomography can be found in Liu *et al* (1999). For a general application, the selection of $\boldsymbol{\tau}$ can be obtained from the Landweber method (Landweber 1951).

References

Abdullah M Z 1993 Electrical impedance tomography for imaging conducting mixture in hydrocyclone separators *PhD Thesis* UMIST

Akaike H 1974 A new look at statistical model identification *IEEE Trans. Autom. Control* **19** 716–30

Arridge S A and Schweiger M 1998 A gradient-based optimization scheme for optical tomography *Opt. Express* **2** 213–26

Barber D C 1990 Quantification in impedance imaging *Clin. Phys. Physiol. Meas.* (Suppl. A) **11** 45–56

Barber D C and Brown B H 1984 Applied potential tomography *J. Phys. E: Sci. Instrum.* **17** 723–33

Boone K, Barber D and Brown B 1997 Review imaging with electricity: report of the European concerted action on impedance tomography *J. Med. Eng. Technol.* **21** 201–32

Breckon W R and Pidcock M K 1987 Mathematical aspects of impedance imaging *Clin. Phys. Physiol. Meas.* (Suppl. A) **8** 77–84

Brown B H and Segar A D 1985 Applied potential tomography: data collection problems *Proc. IEE Int. Conf. on Electric and Magnetic field in Med. And Biol.* pp 79–82

Carey G F (ed) 1989 *Parallel Computing: Methods, Algorithms and Applications* (New York: Wiley)

Cheney M, Isaacson D, Newell J G, Simake S and Goble J 1990 NOSER: an algorithm for solving the inverse conductivity problem *Int. J. Imaging Syst. Technol.* **2** 66–75

Cheng K S, Isaacson D, Newell J C and Gisser D G 1989 Electrode models for electric current computed tomography *IEEE Trans. Biomed. Eng.* **36** 918–24

Cobbold R S C 1974 *Transducers for Biomedical Measurements: Principles and Applications* (New York: Wiley-Interscience)

Geselowitz D B 1971 An application of electrocardiographic lead theory to impedance plethysmography *IEEE Trans. Biomed. Eng.* **18** 38–41

Golub G H and Van Loan C F 1989 *Matrix Computations* 2nd edn (Baltimore, MD: John Hopkins University Press)

Hua P, Woo E J, Webster J G and Tompkins W J 1993 Using compound electrodes in electrical impedance tomography *IEEE Trans. Biomed. Eng.* **40** 29–34

Holden P J, Wang M, Mann R, Dickin F J and Edwards R B 1998 Imaging stirred-vessel macromixing using electrical resistance tomography *AIChE* 780–90

Ider Y Z, Gerber N G, Ataler E and Tosun H 1990 Electrical impedance tomography of translationally uniform cylindrical objects with general cross-sectional boundaries *IEEE Trans. Med. Imaging* **9** 49–59

Jennings A and McKeown J J 1992 *Matrix Computation* (Chichester: Wiley)

Kotre C J 1994 EIT image reconstruction using sensitivity weighted filtered back-projection *Physiol. Meas.* **15** A125–36

Landweber L 1951 An iterative formula for Fredholm integral equations of the first kind *Am. J. Math.* **73** 615–24

Lehr J 1972 A vector derivation useful in impedance plethysmographic field calculations *IEEE Trans. Biomed. Eng.* **19** 156–7

Lionheart W R B 2001 Regularization, constraints and iterative reconstruction algorithms for EIT *3rd EPSRC Engineering Network Meeting Scientific Abstracts* (London: UCL)

Liu S, Fu L and Yang W Q 1999 Optimization of an iterative image reconstruction algorithm for electrical capacitance tomography *Meas. Sci. Technol.* **10** L37–9

Marquardt B W 1963 An algorithm for least-squares estimation of nonlinear parameters *SIAM J. Appl. Math.* **11** 431–41

Mavros P 2001 Flow visualization in stirred vessels—a review of experimental techniques *Trans. IChemE.* **79** A 113–27

Murai T and Kagawa Y 1985 Electrical impedance computed tomography based on a finite element model *IEEE Trans. Biomed. Eng.* **32** 177–84

Pidcock M K 1994 Analysing the importance of electrode modelling in electrical impedance tomography *SIAM J. Appl. Math.* **52** 1012–22

Player M A, Weereld J van, Allen A R and Collie D A L 1999 Truncated-Newton algorithm for three-dimensional electrical impedance tomography *Electron. Lett.* **35** 2189–91

Pollak V 1974 An equivalent diagram for the interface impedance of metal needle electrodes *Med. Biol. Eng.* 454–9

Press W H, Teukolsky S A, Vettering W T and Flannery B P 1992 *Numerical Recipes* (New York: Cambridge University Press)

Reid J K 1971 On the method of conjugate gradients for the solution of large sparse systems of linear equations *Large Sparse Sets of Linear Equations* ed J K Reid (London: Academic)

UMIST 2000 EIT and diffuse optical tomography reconstruction software (EIDORS) www.ma.umist.ac.uk/bl/eidors

Vauhkonen M *et al* 2000 A matlab toolbox for the EIDORS project to reconstruct two- and three-dimensional EIT images *2nd EPSRC Engineering Network Meeting Scientific Abstracts* (London: UCL Press)

Vauhkonen M, Vadasz D, Karjalainen P A, Somersalo E and Kaipio J P 1998 Tokhonov regularization and prior information in Electrical Impedance Tomography *IEEE Trans. Med. Imaging* **17** 285–93

Vauhkonen P J, Vauhkonen M, Savolainen T and Kaipio P 1999 Three-dimensional electrical impedance tomography based on the complete electrode model *IEEE Trans. Biomed. Eng.* **46** 1150–60

Wang M 1994 Electrical impedance tomography n conducting walled process vessels *PhD Thesis* UMIST

Wang M 1999 Three-dimensional effects in electrical resistance tomography *Proc. 1st World Congress on Industrial Process Tomography* (Buxton: VCIPT) pp 410–5

Wang M, Dickin F J and Williams R A 1995a Modelling and analysis of electrically conducting vessels and pipelines in electrical resistance process tomography *IEE Proc. Sci. Meas. Technol.* **142** 313–22

Wang M, Dickin F J and Williams R A 1995b The grouped node technique as a means of handling large electrode surfaces in electrical impedance tomography *Physiol. Meas.* **16** A219–26

Wang M, Mann R and Dickin F J 1996 A Large scale tomographic sensing system for mixing processes *Proc. IWISP'96 (for 3rd Int. Workshop on Image and Signal Processing Advances in Computational Intelligence in Manchester)* (Amsterdam: Elsevier) pp 647–50

Wang M, Mann R and Dickin F J 1999 Electrical resistance tomographic sensing systems for industrial applications *Chem. Eng. Commun.* **175** 49–70

Williams R A and Beck M S (ed) 1995 *Process Tomography—Principles, Techniques and Applications* (Woburn, MA: Butterworth-Heinemann)

Woo E J, Hua P, Webster J G and Tompkins J 1993 A robust image reconstruction algorithm and its parallel implementation in electrical impedance tomography *IEEE Trans. Med. Imaging* **12** 137–46

Yang W Q, Spink D M, York T A and McCann H 1999 An image-reconstruction algorithm based on Landweber's iteration method for electrical-capacitance tomography *Meas. Sci. Technol.* **10** 1065–9

Yorkey T J, Webster J G and Tompkins W J 1987 Comparing reconstruction algorithm for electrical impedance tomography *IEEE Trans. Biomed. Eng.* **34** 843–51